Astronomy
&
Astrophysics

Jet/cloud collision, 3D gasdynamic simulations of HH 110

A. C. Raga[1], E. M. de Gouveia Dal Pino[2], A. Noriega-Crespo[3], P. D. Mininni[4], and P. F. Velázquez[1]

[1] Instituto de Ciencias Nucleares, UNAM, Ap. 70-, 04510 D. F., México
  e-mail: `pablo@nuclecu.unam.mx`
[2] Instituto de Astronomia, Geofisica e Ciencias Atmosfericas, Universidade de São Paulo, R. do Matão 1226,
  055-08-090 São Paulo, SP, Brasil
  e-mail: `dalpino@astro.iag.usp.br`
[3] SIRTF Science Center, California Institute of Technology, IPAC 100-22, Pasadena, CA 91125, USA
  e-mail: `alberto@ipac.caltech.edu`
[4] Departamento de Física, Facultad de Ciencias Exactas y Naturales, Universidad de Buenos Aires,
  Ciudad Universitaria, 1428 Buenos Aires, Argentina
  e-mail: `mininni@df.uba.ar`

Abstract. We present 3D, gasdynamic simulations of jet/cloud collisions, with the purpose of modelling the HH 270/110 system. From the models, we obtain predictions of Hα and H$_2$ 1–0 s(1) emission line maps, which qualitatively reproduce some of the main features of the corresponding observations of HH 110. We find that the model that better reproduces the observed structures corresponds to a jet that was deflected at the surface of the cloud ~1000 yr ago, but is now boring a tunnel directly into the cloud. This model removes the apparent contradiction between the jet/cloud collision model and the lack of detection of molecular emission in the crossing region of the HH 270 and HH 110 axes.

Key words. ISM: Herbig-Haro objects – ISM: jets and outflows – ISM: kinematics and dynamics – ISM: individual (HH 110) – shock waves

1. Introduction

The Herbig-Haro (HH) jet HH 110 (discovered by Reipurth & Bally 1986) is the best observed example of a possible HH jet/dense cloud collision. Reipurth et al. (1996) have interpreted the rather unique, collimated but quite chaotic structure of HH 110 as the result of a deflection of the faint HH 270 jet through a collision with a dense cloud.

The evidence presented by Reipurth et al. (1996) for this interpretation can be summarized as follows:

– no stellar source has been detected aligned with the HH 110 jet;
– the HH 270 jet (ejected from a detected IR and radio source, see Rodríguez et al. 1998) points towards the beginning of the HH 110 jet;
– the proper motions of HH 270 and HH 110 have an approximately 2 to 1 ratio, which is completely consistent with the ≈60° deflection angle defined by the locci of the two jets (the flow approximately lying on the plane of the sky).

This last statement can be understood as follows. When a radiative jet hits the surface of a dense cloud at an incidence angle ϕ (between the incident jet axis and the cloud surface), the normal component of the jet velocity is stopped in a radiative shock, and the jet continues to flow parallel to the surface (conserving the component of the incident jet velocity parallel to the surface). Therefore, the velocity $v_{\rm def}$ of the deflected jet is approximately equal to the projection of the incident jet velocity $v_{\rm inc}$ along the surface of the dense cloud. Therefore, $v_{\rm def} \approx v_{\rm inc} \cos\phi$. One can straightforwardly see that the proper motions and deflection angle defined by HH 270 and HH 110 (see above) do satisfy this condition.

This result led Raga & Cantó (1995) to study the dynamics of the collision of a radiative, HH jet with the surface of a dense cloud. These authors presented an analytic model and plane, 2D simulations of the early stages of such an interaction, and found that the general characteristics of the HH 270/110 system could be explained in terms of such a model. The main problem found with the models is that in a rather short timescale, the incident jet starts to perforate the obstacle, and the deflected jet beam is then pinched off. In order to obtain a long enough timescale for the production of the deflected jet, it is necessary to have a very high cloud-to-jet density ratio.

Raga & Cantó (1995) suggested that this problem might be overcome if the incident jet did not have a completely straight jet beam, so that the impact point would roam over the surface of the dense cloud.

The regime in which the jet has punched a hole through a cloud was described by Cantó & Raga (1996) and Raga & Cantó (1996). If the cloud is stratified, the path of the jet through the cloud is curved, though the curvature is important only if the radius of the cloud is comparable to the jet radius. 3D gasdynamic simulations of the penetration of a jet into and through a dense, stratified cloud were carried out by de Gouveia Dal Pino (1999).

Finally, Hurka et al. (1999) have studied the bending of the beam of a 3D MHD, non-radiative jet by a magnetic field with a strong gradient (as would be found at the surface of a dense cloud). These authors show that this effect would help to increase the timescale over which the jet/cloud surface interaction takes place, before the deflected jet is pinched off.

In the present paper, we discuss 3D gasdynamic simulations of the interaction of a radiative jet with the surface of a dense cloud. We show the results from two simulations with different assumptions for the incident jet:

- that the jet is ejected with a constant direction and velocity;
- that it is produced with a precessing outflow direction and a sinusoidally varying velocity.

Through a comparison of these two simulations, we can evaluate the effect of a "roving" impact point on the production of the deflected jet.

Our simulations include a treatment of the dissociation and ionization of the gas. Therefore, we can use the results to obtain predictions of atomic and molecular lines, which we directly compare with previously published images of HH 110.

In particular, we compute predicted maps in the H_2 1–0 s(1) line. This is of interest because the morphology of HH 110 in this IR line is quite strikingly different from its morphology in atomic/ionic lines. Davis et al. (1994) and Noriega-Crespo et al. (1996) found that the H_2 emission is much better collimated, and lies along one of the edges of the HH 110 jet beam. This led Noriega-Crespo et al. (1996) to present a simple model of the molecular emission as coming from material from the dense cloud which is entrained by the jet as it brushes past the cloud surface. Our present simulations allow us to make a more definite assesment of whether or not such a mechanism actually succeeds in explaining the molecular emission of HH 110.

We should point out that Choi (2001) presents HCO^+ emission maps, in which he detects emission in the HH 270/110 region, but not around the "point of impact" in which the "incident" HH 270 jet is presumably redirected into the "deflected" HH 110 jet. This result leads him to suggest that HH 110 might actually not be the result of a jet/cloud collision, but that it could instead be a "straight" jet ejected from a low luminosity, undetected stellar source which is presumably more or less aligned with the direction of the HH 110 flow. In the conclusions, we discuss the possible ways of reconciling the jet/cloud interaction model with the observations of Choi (2001) which are suggested by our 3D gasdynamic simulations.

2. The numerical simulations

2.1. General features

We have carried out 3D gasdynamic simulations of jet/cloud interactions with the yguazú-a adaptive grid code. This code integrates the 3D (or 2D) gasdynamic equations together with a set of continuity equations for atomic/ionic or chemical species. The details of the gasdynamic and the adaptive grid algorithms have been presented by Raga et al. (2000), and tests of the code are given by Sobral et al. (2000) and Raga et al. (2000).

For the present simulations, we have used the following set of species: H_2, H I and II, C II, III and IV, and O I, II and III (with abundances by number relative to hydrogen: $y_C = 6.6 \times 10^{-4}$ and $y_O = 3.3 \times 10^{-4}$). For the atomic/ionic reactions, we have included the collisional ionization (from Cox 1970), radiative+dielectronic recombination (from Aldrovandi & Péquignot 1973, 1976) and O/H charge exchange processes. The H_2 dissociation and cooling has been included in the same way as in Raga et al. (1995). The cooling associated with the atomic/ionic species has been included as described in Appendix A.

We have computed two jet/cloud interaction models, which share the following characteristics. In both models, an initially atomic jet (except for C, which is singly ionized) of number density $n_j = 50$ cm^{-3} and temperature $T_j = 1000$ K interacts with a spherical, homogeneous molecular cloud (with all H in the form of H_2) of number density $n_c = 5000$ cm^{-3} and $T_c = 1$ K. The cloud is surrounded by a homogeneous, neutral environment of density $n_{env} = 10$ cm^{-3} and temperature $T_{env} = 1000$ K. Therefore, the jet to cloud (mass) density ratio is $\rho_j/\rho_c = 1/100$.

In both simulations, the cloud has a $r_c = 4 \times 10^{17}$ cm radius, and the jet has an initial, top-hat cross section of radius $r_j = 1.5 \times 10^{16}$ cm. The jet is injected at $(x, y, z) = (0, 0, 0)$ with the outflow axis in the z-direction. Free outflow conditions are applied on all of the outer boundaries of the computational domain, except for the $z = 0$ plane, on which a reflection condition is imposed outside of the injection jet cross section.

The computations are carried out on a 5-level, binary adaptive grid (the two coarsest levels being defined over the full computational domain, see Raga et al. 2000) with a maximum resolution (along the three axes) of 3.91×10^{15} cm. The highest resolution grid is only allowed in the regions occupied either by jet or by cloud material (which are traced by advecting a passive scalar), so that the maximum resolution allowed in the environmental material is only of 7.81×10^{15} cm.

We have then computed two models, one with a jet with time-independent injection conditions (model A), and one with a precessing, variable ejection velocity jet (model B). These two models are discussed in the following two subsections.

2.2. Jet with time-independent injection (model A)

In this simulation, the jet is injected parallel to the z-axis, with a constant $v_j = 300$ km s^{-1} injection velocity. The computational domain extends from $-4.5 \times 10^{17} < x < 0.5 \times 10^{17}$ cm, $-2.5 \times 10^{17} < y < 2.5 \times 10^{17}$ cm and $0 < z < 5 \times 10^{17}$ cm.
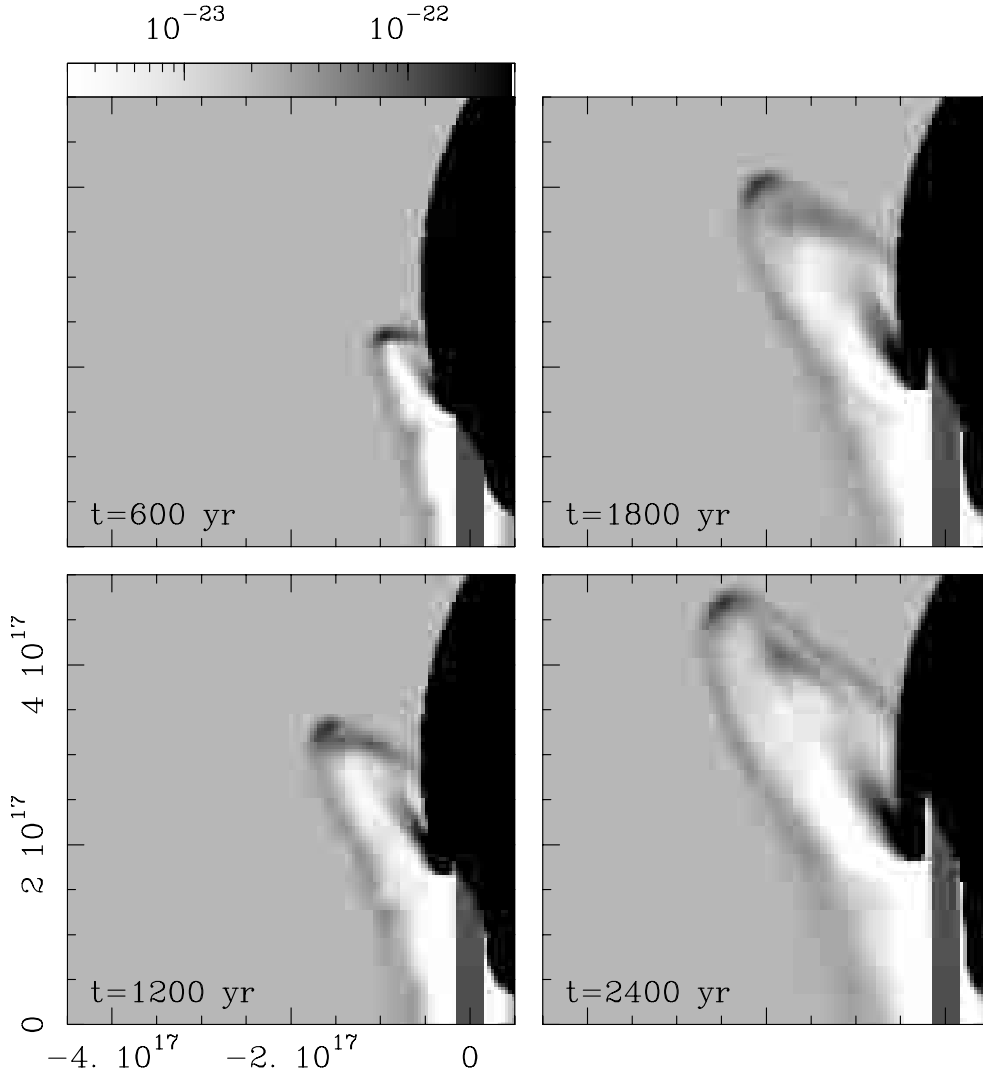
Fig. 1. Time sequence of the density stratifications obtained from model A. The density stratifications on the $y = 0$ plane (which includes the outflow axis and the centre of the spherical cloud) are shown for different integration times (as indicated at the bottom left of each plot). The densities are depicted with a logarithmic greyscale, with the values given (in g cm^{-3}) by the bar on the top left of the figure. The x (horizontal) and z (vertical) axes are labeled in cm.

The centre of the spherical cloud is placed at $(x_c, y_c, z_c) = (3.5, 0, 3) \times 10^{17}$ cm, so that the jet has a glancing collision with the surface of the cloud.

Figure 1 shows a time series (spanning an integration time of $t = 2400$ yr) of the density stratifications on the $y = 0$ plane (this plane includes the outflow axis and the centre of the dense cloud). In this time series one sees the incident jet beam (injected at the origin, and travelling along the z-axis) impinging on the surface of the dense cloud, and being deflected onto a direction towards the top left of the xz-cuts. At $t = 1200$ yr, the jet has already dug a hole into the cloud (this hole becoming deeper at later integration times), and the deflected jet beam basically becomes cut off at its base. At this time, the jet/cloud impact point lies within, rather than at the surface of the cloud. However, the material deflected by the cloud surface at earlier times continues to travel away from the cloud, leaving a complex "wake", joining it to the point at which the incident jet impacted the cloud surface.

In order to illustrate the configurations adopted by the adaptive grid, Fig. 2 shows the temperature stratification and the adaptive grid structure on the $y = 0$ plane obtained for $t = 2400$ yr. It is clear from this figure that the higher resolution is not allowed on the regions occupied by environmental gas, so that the leading bow shock is only resolved at the second highest resolution level.
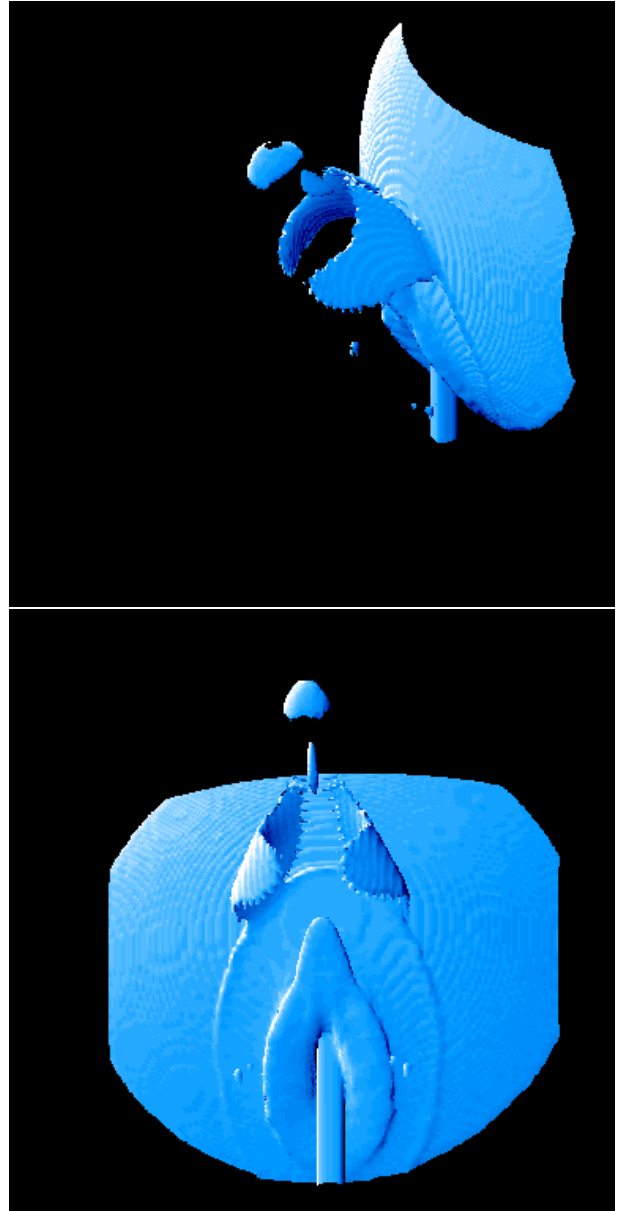
Figure 2 also shows the following. We have integrated an advection equation for a passive scalar ψ. This scalar has been given a value of $\psi = 1$ for the jet, 2 for the dense cloud, and -1 for the surrounding environment. In the plot showing the adaptive grid, we have also drawn two contours on the stratification of the passive scalar corresponding to values $\psi = 0$ (outer contour) and $\psi = 1.5$ (inner contour). The region in between the two contours corresponds to the jet material (which has $\psi = 1$). From Fig. 2 it is then clear that the jet material occupies the injection region and the hole in the cloud, as well as a "plug" of material (at $(x, y) \approx (-2.5, 4.5) \times 10^{17}$ cm) with wings which

10^3 10^4
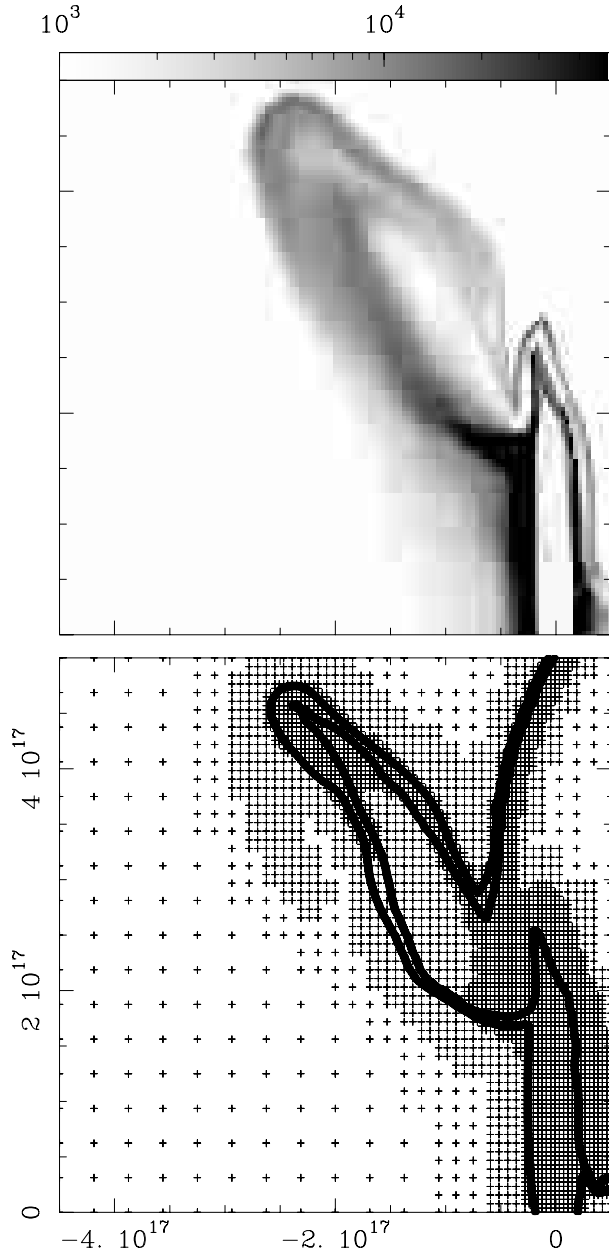
Fig. 2. Temperature stratification (top) and adaptive grid structure (bottom) on the $y = 0$ plane obtained from model A for a $t = 2600$ yr integration time. The temperature stratification is depicted with a logarithmic greyscale with the values given (in K) by the bar on the top of the figure. In the bottom plot, two thick lines separating the jet, cloud and environmental material are shown (see the text). These lines show two values of the passive scalar: $\psi = 0$ (outer contour) and $\psi = 1.5$ (inner contour).

Fig. 3. Constant density surface (corresponding to a $n = 20$ cm^{-3} number density of atomic nuclei) from model A for a $t = 2600$ yr integration time. The two graphs show the surface as seen from two different directions.

penetrating into the cloud, part of the bow shock, the denser region of the deflected jet beam and the entrained molecular gas material (which forms a structure which surrounds the incident jet, and has an elongation in the direction of the deflected jet beam).

extend towards the jet/cloud impact point. The region in between the wings is filled in by a tongue of cloud material which has been swept into the deflected jet flow. We find that this entrained cloud material has interesting observational properties, which are described in Sect. 3.

The structure of this dense tongue is more clearly seen in Fig. 3, which shows a constant density 3D surface (corresponding to a $n = 20$ cm^{-3} number density of atomic nuclei) obtained for a $t = 2600$ yr integration time. This figure shows the jet

2.3. Precessing, variable ejection velocity jet (model B)

We have computed a second simulation, in which the ejection direction precessses around the jet axis. The precession cone has an $\alpha = 5°$ half-opening angle, and a $\tau_p = 400$ yr precession period. Also, the jet is injected with a constant density ($n_j = 50$ cm^{-3}, see Sect. 2.1), but with a sinusoidally
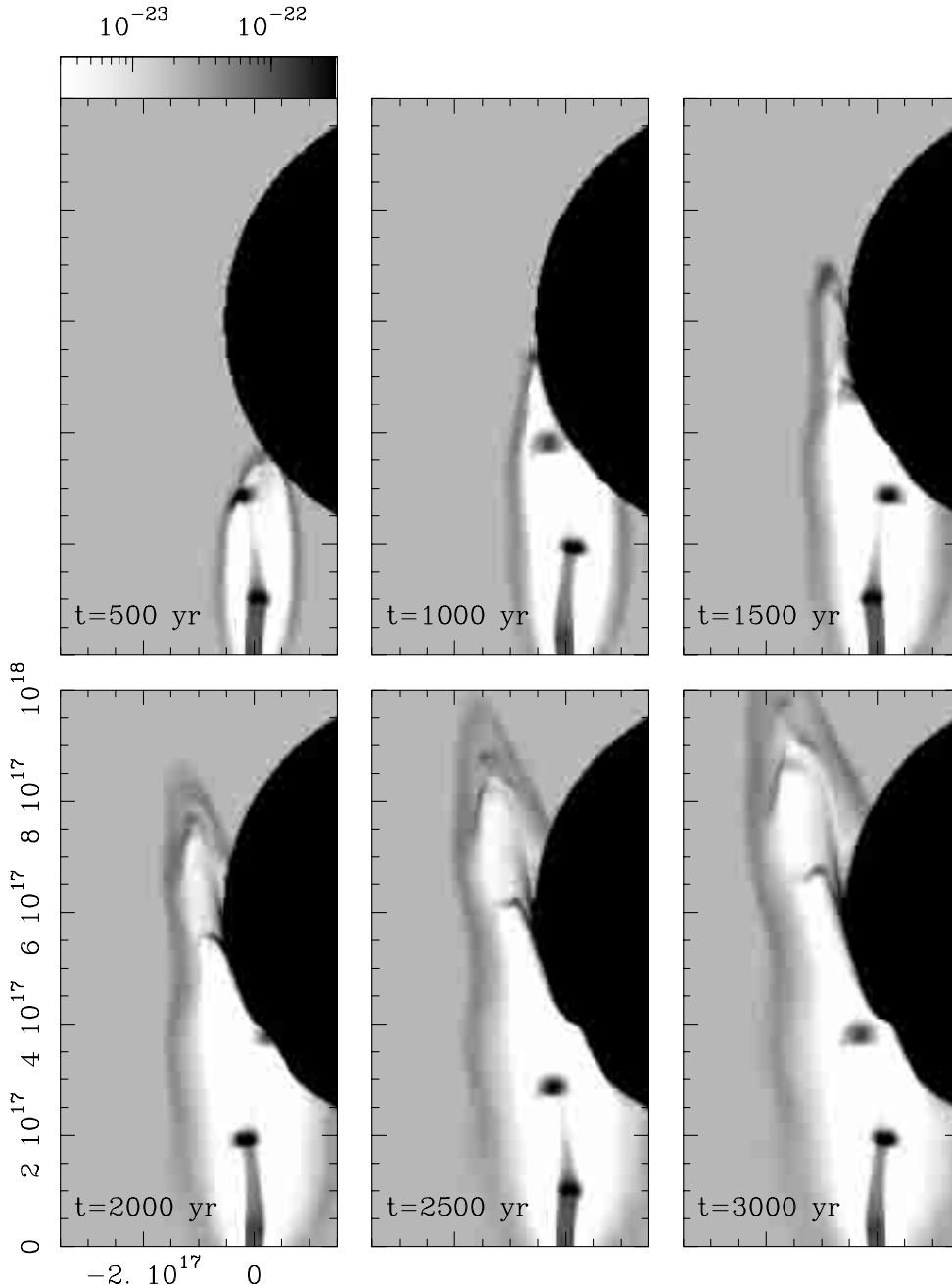
Fig. 4. Time sequence of the density stratifications obtained from model B. The density stratifications on the $y = 0$ plane (which includes the outflow axis and the centre of the spherical cloud) are shown for different integration times (as indicated at the bottom left of each plot). The densities are depicted with a logarithmic greyscale, with the values given (in g cm^{-3}) by the bar on the top left of the figure. The x (horizontal) and z (vertical) axes are labeled in cm.

varying ejection velocity $v_j(t) = (300 + 80 \sin 2\pi t/\tau_v)$ km s^{-1}, with a $\tau_v = 200$ yr period.

For this simulation, we choose a computational domain with the same extent as the one of model A along the x and y axis (but with a diferent centering: $-3.5 \times 10^{17} < x < 1.5 \times 10^{17}$ cm and $-2.5 \times 10^{17} < y < 2.5 \times 10^{17}$ cm) but with a larger, $0 < z < 10^{18}$ cm extent along the outflow axis. The center of the spherical cloud is placed at $(x_c, y_c, z_c) = (3.5, 0, 6) \times 10^{17}$ cm. We have chosen to have a larger distance from the point of injection to the jet/cloud collision region in order to allow the internal working surfaces of the jet (which

result from the ejection velocity time-variability) to form before colliding with the dense cloud.

Figure 4 shows a time sequence of the density stratifications obtained on the $y = 0$ plane (which includes the precession axis and the centre of the cloud). In this figure, one sees the internal working surfaces which first form, and then impact the surface of the dense cloud. Because of the precession in the ejection direction, the successive working surfaces impact the cloud at different points. Through a comparison with Fig. 1, it is clear that this effect increases the time that the jet takes to dig a hole into the cloud (and therefore pinching off the
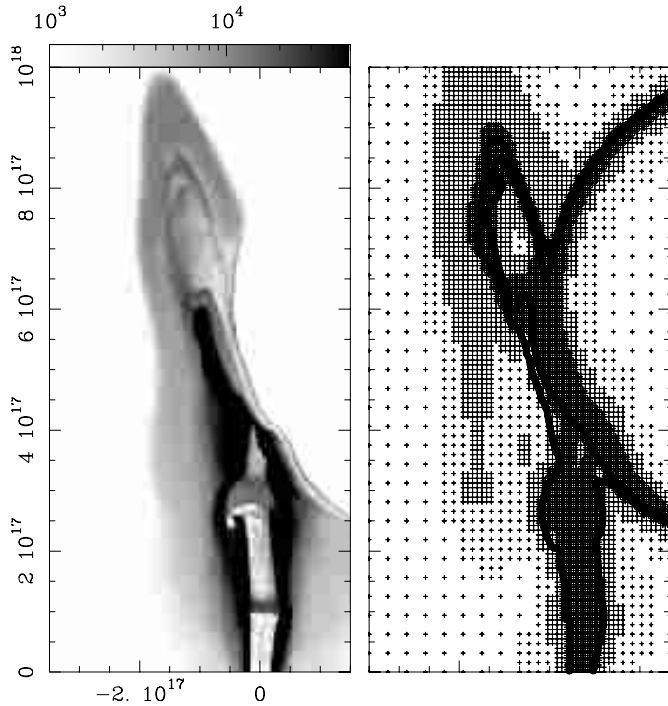
Fig. 5. Temperature stratification (left) and adaptive grid structure (right) on the $y = 0$ plane obtained from model A for a $t = 2500$ yr integration time. The temperature stratification is depicted with a logarithmic greyscale with the values given (in K) by the bar on the top of the figure. In the right hand side plot, two thick lines separating the jet, cloud and environmental material are shown (see the text).

deflected jet beam). In fact, for the $t = 3000$ yr time-integration shown in Fig. 4, the depth of the hole is still smaller than the diameter of the impinging jet (for a similar time frame obtained from model A, the depth of the hole is of approximately two jet diameters, see Fig. 1). Similar results are deduced by analyzing different $y = $ const. cuts through the 3D density stratification.

Figure 5 shows the temperature stratification, and the grid structure on the $y = 0$ plane obtained for a $t = 2500$ yr time-integration (equivalent results for model A are shown in Fig. 2). On the graph with the adaptive grid, we again show the contours that separate the jet, cloud and environmental material (for model A, see Fig. 2 and the discussion at the end of Sect. 2.2). It is clear that model B has a more complex structure than model A, showing a number of condensations of jet material in the "deflected flow" region, which correspond to the different working surfaces that have been deflected on collision with the cloud surface. Interestingly, the center of the deflected flow region is filled with material from the molecular cloud, as is also the case for model A (see Fig. 2).

In the following section, we present predictions of emission line intensity maps carried out from the results of models A and B. These predictions can then be compared directly with the available observations of the HH 270/110 system.

3. Predicted intensity maps

3.1. General considerations

In order to compare the jet/cloud interaction models described in Sect. 2 with the published images of the HH 270/110 system, we have obtained predicted emission line maps from the models. From the computed temperature, density, electron density and H ionization and molecular fractions, we have computed the Hα and H$_2$ 1–0 s(1) (2.12 μm) emission coefficients.

For the Hα emission line coefficient, we have included the recombination cascade and the $n = 1 \rightarrow 3$ collisional excitation (using the corresponding excitation coefficient of Giovanardi & Palla 1989). The H$_2$ 1–0 s(1) coefficient was computed by solving the level population equations according to the prescription of Draine et al. (1983, corrected according to Flower et al. 1986). This is by no means the more accurate calculation of H$_2$ level populations available (see, e.g., Flower & Pineau des Forêts 1999), but it is appropriate given the limited accuracy of our rather low resolution numerical simulations.

We have then computed intensity maps by integrating the emission coefficients along lines of sight. We have assumed that the $y = 0$ plane (which includes the axis of the incident flow and the centre of the cloud) coincides with the plane of the sky. This is probably a reasonable approximation to the orientation of the HH 270/110 flow, since it is known that both HH 270 and HH 110 approximately lie on the plane of the sky (Reipurth et al. 1986).
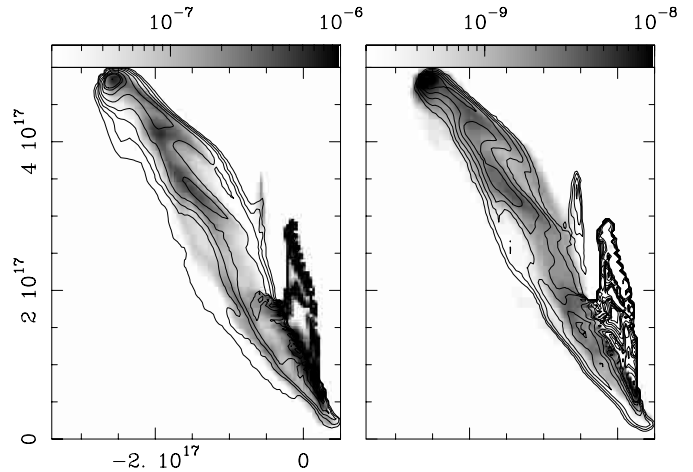
3.2. Intensity maps predicted from model A

In Fig. 6, we show the Hα emission line maps predicted from model A (see Sect. 2.2). From the bottom plot, it is completely clear that the emission is dominated by the region in which the incident jet beam is digging into the cloud. As the optical emission maps of HH 110 do not show this emitting region, we have to conclude that it has to be absorbed by the dust in the dense cloud (at least, if we believe in the jet/cloud interaction model for this object).

In order to illustrate the effect on the Hα maps of such an extinction, we have computed emission maps including this effect (top two maps of Fig. 6). We have computed the maps assuming that the dust extinction coefficient is $\kappa_d = 10^{-20}(n_H/\text{cm}^{-3})$ cm^{-1}, giving a $\tau_d = 40$ optical depth through the radius of the cloud.

We should note that if we use the standard, $\kappa_d = 10^{-21}(n_H/\text{cm}^{-3})$ cm^{-1} dust absorption coefficient, our cloud would have a $\tau_d = 4$ central optical depth. The region on the edge of the cloud into which the jet is penetrating would then have a low optical depth, producing little extinction of the emission from the impact region. This, however, is not a major problem given the fact that the dense cloud present in the HH 270/110 region is by no means either spherical or homogeneous, and could easily produce a large extinction towards the current jet/cloud impact region (which would lie within the cloud).
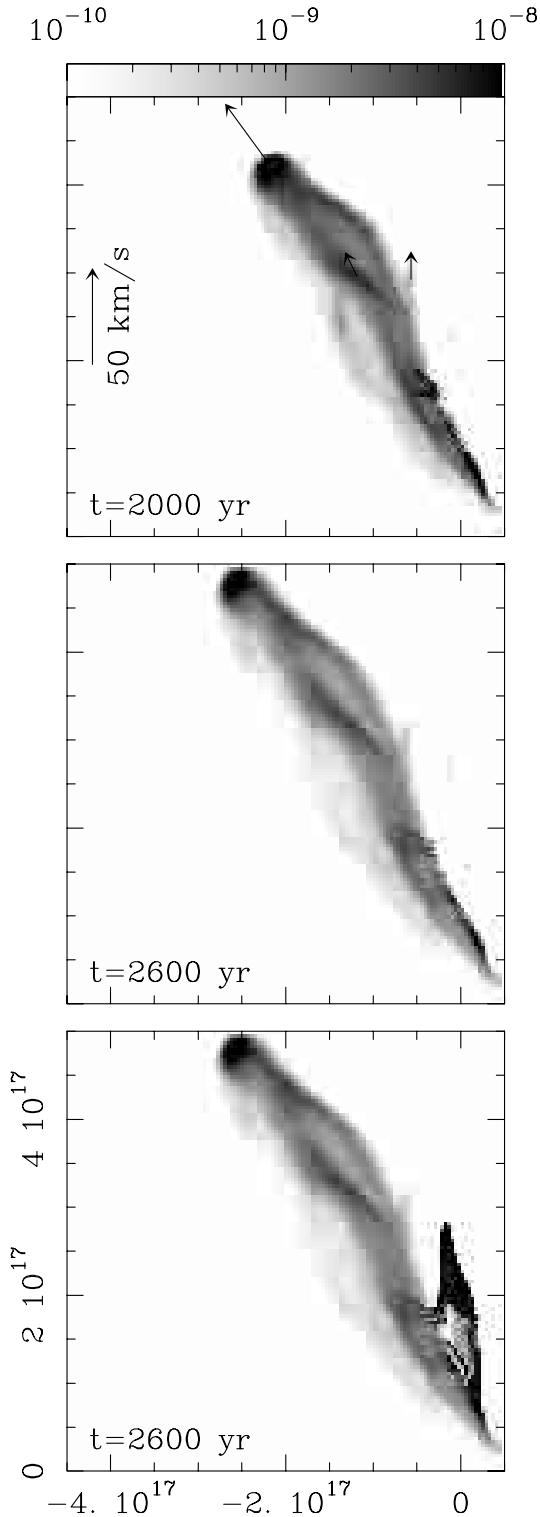
Fig. 6. Hα maps predicted from model A, corresponding to the integration times given on the bottom left of each frame. The maps are depicted with the greyscale given by the bar at the top of the graph (which gives the intensity values in erg cm^{-2} s^{-1} sterad^{-1}). The two top frames have been computed including the dust extinction of the dense cloud (see Sect. 3.2), and the bottom frame shows a map computed without considering this extinction. The proper motions computed from the positions of three intensity maxima (as measured in the t = 2000 and 2600 yr maps) are shown in the top frame. The x (horizontal) and z (vertical) axes are labeled in cm.

Fig. 7. Hα and H$_2$ 1–0 s(1) intensity maps computed from model A for a t = 2600 yr integration time (see Sect. 3.2). The left plot shows the Hα map in factor of 2 contours and the H$_2$ map in the greyscale described by the bar at the top of the plot. The right plot shows the H$_2$ map in factor of 2 contours and the Hα map in gresycale (corresponding to the bar at the top of the plot). The greyscales (given in erg cm^{-2} s^{-1} sterad^{-1} by the corresponding bars) and the contours of the intensity maps of a given line correspond to the same range of intensities. The x (horizontal) and z (vertical) axes are labeled in cm.

The Hα maps obtained from model A (for integration times t = 2000 and 2600 yr) computed with the dust extinction as described above are shown in the two top frames of Fig. 6. It is clear that these maps do present a qualitative similarity to HH 110 (see, e.g., Reipurth et al. 1996).

In agreement with the observations, the emitting region starts with a bright rim (in contact with the surface of the cloud, see Fig. 6) which points to a broader structure (with a complex structure of curved ridges) at larger distances from the impact region. Also, there is a faint emission halo extending parallel to the main emission structure on the side directed away from the dense cloud. This is also in qualitative agreement with the Hα maps of HH 110 (Reipurth et al. 1996).

From the two time frames shown in Fig. 6, we have computed proper motions for the three main intensity maxima seen in the maps. We have also computed proper motions for some of the local maxima in the region in which the emission is in contact with the cloud surface, but the resulting velocities lie between 3 and 8 km s^{-1}, and have not been plotted in Fig. 6.

The proper motions of the knots farther away from the cloud (shown in Fig. 6) have values of 15 to 45 km s^{-1}. These proper motions are substantially lower than the ones measured for the HH 110 knots, as Reipurth et al. (1996) have found values ranging from 35 to 150 km s^{-1}.

In Fig. 7, we show a comparison between the Hα and the H$_2$ 1–0 s(1) intensity maps obtained for t = 2600 yr. For computing the H$_2$ map, we have considered an extinction equal to 1/10 of the visual extinction. This results in only small optical depths towards the current jet/cloud impact region, so that the emission from this region is clearly visible.

The H$_2$ emission in the base of the deflected jet region is much more concentrated towards the surface of the cloud than the Hα emission. This result is in clear qualitative
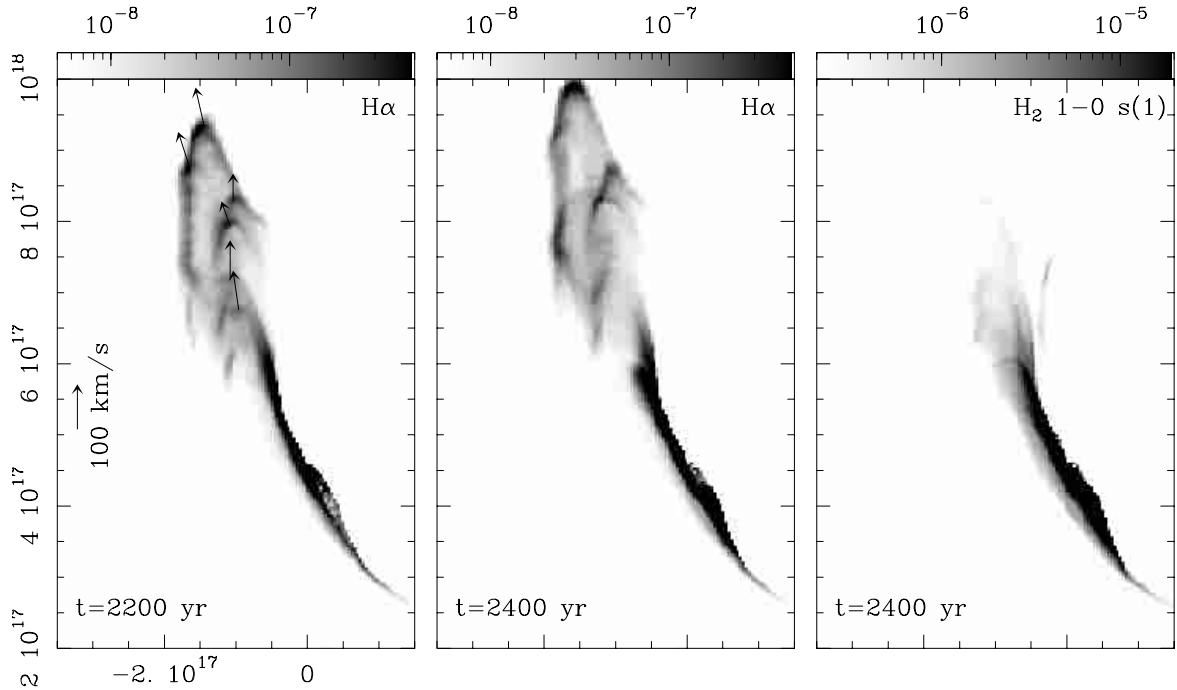
Fig. 8. Intensity maps obtained from model B (see Sect. 3.3). The left and central frames show the Hα maps obtained for two integration times (given on the bottom left of each frame). The right hand side frame shows the H_2 1–0 s(1) map obtained for $t = 2400$ yr. The maps are depicted with the greyscales given (in erg cm^{-2} s^{-1} sterad^{-1}) by the bars on the top of each frame. The left plot shows the proper motions of several intensity maxima, computed from the $t = 2200$ and 2400 yr Hα intensity maps. The x (horizontal) and z (vertical) axes are labeled in cm.

agreement with the morphology observed in HH 110 (Davis et al. 1994; Noriega-Crespo et al. 1996). At larger distances along the deflected jet flow, the H_2 and Hα emission show spatially coincident condensations, again in agreement with the observations of HH 110.

3.3. Intensity maps predicted from model B

In Fig. 8, we show the Hα intensity maps computed from model B for $t = 2200$ and 2400 yr integration times, and the H_2 1–0 s(1) map obtained for $t = 2400$ yr. Because of the fact that the jet/cloud impact region still lies on the surface of the cloud, the effect of the extinction due to the dust present in the cloud is not important, and has not been included. However, the extinction would be important for maps computed for different orientations of the jet/cloud structure with respect to the plane of the sky.

As a result of the precession and ejection velocity time variability of the incident jet (see Sect. 2.3), the emission maps show more complex structures than the ones obtained from model A. In particular, one can clearly see the emission from bow shocks around dense "bullets", which result from the successive internal working surfaces present in the incident jet. Even though the morphology observed in the emission line maps of HH 110 is very complex (see, e.g., Reipurth et al. 1996), it does not appear to have such bow shock structures. Actually, the intensity maps predicted from model A do resemble the structure of HH 110 in a more convincing way.

An interesting feature of model B is that the proper motions of the different intensity maxima (obtained by comparing the $t = 2200$ and 2400 yr Hα intensity maps, see Fig. 8) have values of close to 100 km s^{-1}. These velocities are in better agreement with the ones measured for HH 110 than the ones obtained from model A (see Sect. 3.2 and Reipurth et al. 1996).

4. Conclusions

We have presented two jet/cloud collision 3D gasdynamic simulations: one with an incident jet with time-independent injection conditions (model A), and a second one with a variable velocity, precessing incident jet (model B). A $\rho_c/\rho_j = 100$ cloud to initial jet density ratio has been chosen for both models.

Model A produces a deflection of the jet beam only for a ~500–1000 yr timescale, after which the incident jet starts digging a straight tunnel through the dense cloud. At later times, the deflected jet material continues to travel away from the impact region, leaving behind a complex "wake".

Model B produces a broader jet/cloud impact region as a result of the jet precession. This effect results in a longer timescale for the duration of the jet deflection on the cloud surface (in fact, the jet deflection is still occuring at the end of our $t = 3000$ yr numerical simulation).

Model B is more successful at reproducing the proper motions of HH 110, giving ~100 km s^{-1} velocities for the Hα intensity maxima along the deflected jet beam. Model A gives velocities of ~15–45 km s^{-1}, which are substantially lower than the proper motion velocities of HH 110 (see Reipurth et al. 1996).

This difference between model A and model B is due to two effects. The first effect is that in model A, the jet is deflected only for a ~500–1000 yr timescale, and that this deflected jet material then slows down as it interacts with surrounding, environmental gas. In model B, successive deflected "bullets" (i.e., internal working surfaces) travel into the low density region left behind by the passage of the head of the deflected jet, and do not interact directly with the higher density environment. The second effect is that because of the precession of model B, some of the bullets have trajectories which are more tangential to the surface of the molecular cloud. These more tangential bullets are less deflected, and therefore preserve larger velocities than the ones that have a more normal incidence on the cloud surface (or than the deflected jet of model A).

However, in most other counts, model A is more successful than model B at reproducing the observations of HH 110:

– The general qualitative appearance of the Hα maps is in better agreement with the HH 110 Hα images.
– The features of the H₂ 1–0 s(1) emission and their spatial relation to the Hα emission also are in good qualitative agreement with HH 110.
– The maps that better resemble HH 110 correspond to times (e.g., the $t = 2400$ yr frame of Figs. 1 and 6) in which the impact region is already immersed within the cloud.

This last feature offers an interesting way of reconciling the jet/cloud collision model with the HCO⁺ observations of Choi (2001).

In these observations, no HCO⁺ emission was detected in the region in which the axis of the "incident" HH 270 jet crosses the axis of the "deflected" HH 110. Choi (2001) noted that this appeared to be in disagreement with a jet/cloud collision model for this system, as the cloud shock produced in the impact region should indeed produce HCO⁺ emission.

The situation found in model A, however, could indeed be in agreement with the observations of Choi (2001). In this model, the impact region does not lie in the point in which the incident and deflected jet axes cross, but is instead located further along the axis of the incident jet. Interestingly, Choi (2001) does find substantial HCO⁺ emission West of HH 110, approximately aligned with HH 270.

As we have discussed in Sect. 3.2, the fact that the impact region is not observed optically can in principle be a result of the dust extinction in the dense cloud. Interestingly, some H₂ 1–0 s(1) emission is apparently detected to the West of HH 110 (more or less aligned with HH 270, see Noriega-Crespo et al. 1996), which in principle might be associated with the impact region.

To conclude, we note the two main features of our results:

– We find that the jet/cloud interaction model does reproduce the Hα and H₂ 1–0 s(1) emission observed in HH 110 in a qualitatively successful way.
– Our models show that the lack of a detected impact zone in the incident/deflected jet crossing regions (Choi 2001) is not a major problem for a jet/cloud collision model (as this region could presently be displaced further into the cloud).

Clearly, important questions remain about the more technical aspects of our simulations. In particular, the H₂ emission from the deflected jet comes from molecular cloud material which has been entrained into the jet flow (see Figs. 2 and 5). Even though we find that our models produce H₂ emission structures in agreement with the observations of HH 110, the accuracy of our rather low resolution simulations in reproducing the entrainment process (which gives rise to this emission) is somewhat questionable. Because of this, the present results have to be taken with some caution.

Appendix A: The atomic/ionic cooling rates

For H I and II, C II and III and O I and II, we take the cooling rates (per atom and per electron) tabulated by Raga et al. (1997). In order to simplify the calculation of the cooling rate, we note that the cooling per atom or ion starts to deviate from the low density limit only for electron densities $n_e > 10^4$ cm⁻³. As such electron densities are generally not found in HH objects, one can safely consider only the low density limit.

In this limit, the cooling per atom and per electron is only a function of the temperature, and one can then make simple parametric fits for the cooling due to each of the considered species. The following fits (giving the cooling rate in erg s⁻¹ cm³) have errors smaller than 10% over the full $10^3 \to 10^6$ K range (unless otherwise noted):

1. Collisional excitation of HI

$$\log_{10}\left(\frac{L_{HI}}{n_e n_{HI}}\right) = -50 + 32.3(1-t) - 1180(1-t^{0.0001}), \quad (A.1)$$

with $t = 1590$ K$/T$.

2. Collisional ionisation of HI

$$L_{ion,HI} = n_e n_{HI} q(T)\chi_H, \quad (A.2)$$

where $q(T)$ is the collisional ionisation coefficient and χ_H the ionisation potential of H.

3. Radiative recombination of HII
We have included the classical interpolation formula of Seaton (1959).

4. Collisional excitation of O I (electrons)
$L = L_1 + L_2$ with

$$\log_{10}\left(\frac{L_1}{n_e n_{OI}}\right) = -23.95 + 1.23t_1 + 0.5t_1^{10}, \quad (A.3)$$

$$\log_{10}\left(\frac{L_2}{n_e n_{OI}}\right) = -21.05 + 1.2t_2 + 1.2\,[\max(t_2,0)]^5 , \qquad (A.4)$$

with $t_1 = 1 - 100\,\text{K}/T$ and $t_2 = 1 - 10^4\,\text{K}/T$.

5. Collisional excitation of O I (neutrals)

$$\log_{10}\left(\frac{L}{n_{HI} n_{OI}}\right) = 10.3t + t^8 - 34.4 , \qquad (A.5)$$

with $t = 10\,\text{K}/T$. This interpolation formula fits the computed cooling in the $10 \to 10^5$ K temperature range.

6. Collisional excitation of O II
$L = L_1 + L_2$ with

$$\log_{10}\left(\frac{L_1}{n_e n_{OII}}\right) = 7.9t_1 - 26.8 , \qquad (A.6)$$

$$\log_{10}\left(\frac{L_2}{n_e n_{OII}}\right) = 1.9\,\frac{t_2}{|t_2|^{0.5}} - 20.5 , \qquad (A.7)$$

with $t_1 = 1 - 2000\,\text{K}/T$ and $t_2 = 1 - 5 \times 10^4\,\text{K}/T$.

7. Collisional excitation of C II

$$\log_{10}\left(\frac{L_1}{n_e n_{CII}}\right) =$$
$$-23.65 + 1.2\,[\max(t-2),0]^{[1.5-0.25\max(t-4,0)]} , \qquad (A.8)$$

with $t = \log_{10} T$ [K].

8. Collisional excitation of C III

$$\log_{10}\left(\frac{L_1}{n_e n_{CIII}}\right) = -20.8 + 3.9(t-4) - 1.37(t-4)^2 , \qquad (A.9)$$

with $t = \min(\log_{10} T\,[\text{K}], 5.4)$.

9. Parametrized cooling for OIII
We have replaced the real cooling due to collisional excitation of OIII with a function that resembles the coronal ionisation equilibrium for $T > 10^5$ K. In this way, the computed cooling has a transition to the coronal equilibrium cooling when all O becomes OIII and all C becomes CIV (with which no cooling is computed). The adopted functional form is $L = L_1 + L_2$ with

$$\log_{10}\left(\frac{L_1}{n_e n\, y_{OIII}}\right) = -21.4 - 3.5(t-5.4)^2 , \qquad (A.10)$$

$$\log_{10}\left(\frac{L_2}{n_e n\, y_{OIII}}\right) = -21.7 - 0.7(t-6.5)^2 , \qquad (A.11)$$

where $t = \log_{10} T$ [K] and y_{OIII} is the OIII ionisation fraction.

References

Aldrovandi, S. M. V., & Péquignot, D. 1973, A&A, 25, 137
Aldrovandi, S. M. V., & Péquignot, D. 1976, A&A, 47, 321
Cantó, J., & Raga, A. C. 1996, MNRAS, 280, 559
Choi, M. 2001, ApJ, 550, 817
Cox, D. 1970, Ph.D. Thesis (Univ. of California)
Davis, C. J., Mundt, R., & Eislöffel, J. 1994, ApJ, 437, L55
Draine, B. T., Roberge, W. G., & Dalgarno, A. 1983, ApJ, 264, 485
Flower, D. R., Pineau des Forêts, G., & Hartquist, T. W. 1986, MNRAS, 218, 729
Flower, D. R., & Pineau des Forêts, G. 1999, MNRAS, 308, 271
Giovanardi, C., & Palla, F. 1989, A&AS, 77, 157
de Gouveia Dal Pino, E. M. 1999, ApJ, 526, 862
Hurka, J. D., Schmid-Burgk, J., & Hardee, P. E. 1999, A&A, 343, 558
Noriega-Crespo, A., Garnavich, P. M., Raga, A. C., Cantó, J., & Böhm, K. H. 1996, ApJ, 462, 804
Raga, A. C., & Cantó, J. 1995, RMxAA, 31, 51
Raga, A. C., Taylor, S. D., Cabrit, S., & Biro, S. 1995, A&A, 833, 843
Raga, A. C., & Cantó, J. 1996, MNRAS, 280, 567
Raga, A. C., Mellema, G., & Lundqvist, P. 1997, ApJS, 109, 517
Raga, A. C., Navarro-González, R., & Villagrán-Muniz, M. 2000, RMxAA, 36, 67
Raga, A. C., Sobral, H., Villagrán-Muniz, M., Navarro-González, R., & Masciadri, E. 2001, MNRAS, 324, 206
Reipurth, B., & Bally, J. 1986, Nature, 320, 336
Reipurth, B., Raga, A. C., & Heathcote, S. 1996, AJ, 311, 989
Rodríguez, L. F., Reipurth, B., Raga, A. C., & Cantó, J. 1998, RMxAA, 34, 69
Seaton, M. J. 1959, MNRAS, 119, 81
Sobral, H., Villagrán-Muniz, M., Navarro-González, R., & Raga, A. C. 2000, App. Phys. Lett., 77, 3158